Chinese Chemical Letters 36 (2025) 110397

Contents lists available at ScienceDirect

Chinese Chemical Letters

journal homepage: www.elsevier.com/locate/cclet

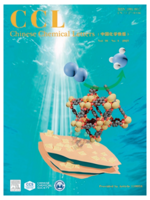

MOF-derived NiCo bimetallic cocatalyst for enhanced photocatalytic overall water splitting

Liang Dong, Jingkuo Qu, Tuo Zhang, Guanghui Zhu, Ningning Ma, Chang Zhao, Yi Yuan, Xiangjiu Guan*, Liejin Guo*

International Research Center for Renewable Energy, State Key Laboratory of Multiphase Flow in Power Engineering, Xi'an Jiaotong University, Xi'an 710049, China

ARTICLE INFO

Article history:
Received 14 June 2024
Revised 29 August 2024
Accepted 30 August 2024
Available online 31 August 2024

Keywords:
Photocatalysis
Overall water splitting
Non-noble metals
Alloy
Cocatalyst

ABSTRACT

The development of stable and efficient non-noble metal cocatalysts has arisen as a promising yet challenging endeavor in the context of photocatalytic overall water splitting. In this study, NiCo alloy cocatalysts were synthesized with nickel/cobalt metal organic framework (NiCo-MOF) as source of nickel and cobalt. Systematic characterization results demonstrate the successful deposition of alloy cocatalysts onto the surface of $SrTiO_3$. The prepared $SrTiO_3$ loaded NiCo-alloy can generate hydrogen and oxygen in a stoichiometric ratio for photocatalytic overall water splitting, achieving an apparent quantum yield of 11.9% at 350 ± 10 nm. Theoretical calculations indicate that the introduction of cobalt has a beneficial regulatory effect on the hydrogen evolution sites of Ni, reducing the free energy of H adsorption. The synergistic catalytic effect of bimetallic catalysts contributes to enhancing photocatalytic activity and stability. This study offers constructive insights for the development of high-efficiency and cost-effective cocatalyst systems.

With the widespread use of fossil fuels, environmental pollution and energy scarcity issues have become increasingly severe [1,2]. The exploitation and utilization of clean and renewable energy is receiving wider attention than ever before. Hydrogen is considered to be the most desirable secondary energy source with high energy density, easy storage and transportation, no carbon emission and renewable [3-6]. The research and development of efficient and low-cost hydrogen-production technology has become a research hotspot in recent years. Solar-driven photocatalytic splitting of water for hydrogen production has the advantages of mild reaction, no additional energy input, and non-polluting products, which is considered as one of the most promising ways [1,7,8]. Yet, practical water splitting systems rely on the development of stable and efficient photocatalysts [9].

Due to its suitable position of the conduction and valence bands, $SrTiO_3$ has received wide attention in the field of photocatalysis, especially on photocatalytic overall water splitting. The research of $SrTiO_3$ as photocatalyst has made great progress recently. Typically, Domen *et al.* reported Al-doping $SrTiO_3$ (STO) with apparent quantum yield (AQY) of 96% at 365 nm with co-loading Rh/Cr_2O_3 and CoOOH cocatalysts [10]. This groundbreaking research has shown that the surface energy band bending, the suppression of Ti^{3+} defects, and the co-catalyst-modulated carrier space separation and surface reactions together guarantee the photocatalytic performance of STO [10,11]. Further investigation realized a demonstration application at 100 m^2 scale with solar-to-hydrogen conversion efficiency of 0.76% using STO [3]. Recent related studies have revealed the key factors affecting the performance of STO from the perspective of carrier dynamics [12,13], showing that Al doping prolongs the carrier lifetime, while Rh loading is crucial for photogenerated electron migration to the surface of STO for hydrogen evolution reaction. Tian and Fang *et al.* investigated the modulation mechanism of the internal defects in STO in terms of Al doping amount and molten salt medium, respectively [11,14].

As indicated by previous reports, photocatalytic hydrogen production from overall water splitting currently relies on noble metal loading, potentially increasing the cost of application [10,15-18]. The development of noble-metal-free co-catalyst systems are highly desirable to realize the large-scale application of photocatalysis [4,19-22]. However, the performance of single-metal co-catalysts is still limited [7,15]. Recently, alloy co-catalysts with synergistic effects for photocatalysis, unique microstructures

---

* Corresponding authors.
E-mail addresses: xj-guan@mail.xjtu.edu.cn (X. Guan), lj-guo@mail.xjtu.edu.cn (L. Guo).

https://doi.org/10.1016/j.cclet.2024.110397

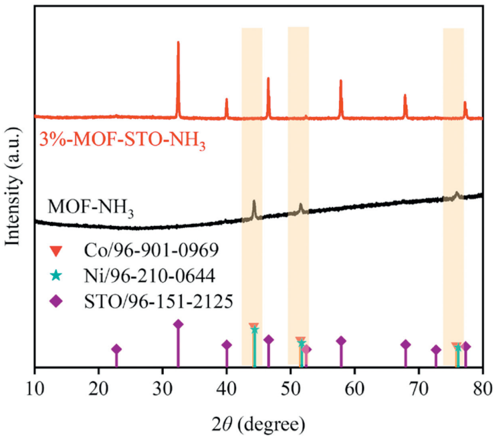

Fig. 1. XRD patterns of 1%-MOF-STO-NH$_3$ and MOF-NH$_3$.

and suitable work functions have attracted increasing attention [7,23-25]. Double-non-noble-metal cocatalysts, such as NiCd [26], CuNi [27], NiMo [28], CoNi [29] and FeCu [30], have been used as co-catalysts for photocatalytic water splitting at the presence of sacrificial agents. The injection of heterogeneous metals can modulate the work function of the base metal, which facilitates the adsorption energy of H_2O and H [27,31]. Meanwhile, the bimetallic synergistic effect can improve the stability during photocatalytic process. In recent studies, nickel-cobalt alloys have shown excellent performance as catalysts in electrocatalysis for hydrogen evolution reaction [32,33] and oxygen evolution reaction [34]. However, preparation and loading approaches for alloy co-catalyst with earth abundant metals and the overall water splitting performance need further investigation and improvement [35-37]. Metal-organic frameworks (MOFs), as a kind of porous structure composed of metal ions and organic ligands with unique microscopic morphology and flexible tunability, have attracted much attention in the field of catalysis [38]. Ionic doping *in situ* during MOF formation with the help of metal-organic ligand interactions enables a more rational and homogeneous spatial distribution of the bimetallic atoms, which could facilitate the formation of alloy.

In this work, NiCo-alloy co-catalysts prepared with MOF as precursor have superior catalytic performance and more attractive stability than other approaches. The prepared STO loaded with noble-metal-free alloy can produce hydrogen and oxygen for photocatalytic overall water splitting in stoichiometric ratio, which could achieve AQY of 11.9% at 350 ± 10 nm. Characterization and theoretical calculations demonstrate the synergistic effect of bimetallic alloy for photocatalytic reactions. Meanwhile, the introduction of Co into Ni to form NiCo-alloy, the H adsorption energy of Ni sites was significantly reduced, which was more suitable for H adsorption. This work is expected to provide a low-cost and high-performance co-catalyst synthesis and loading scheme.

The crystal structure and composition of the prepared sample are determined by powder X-ray diffraction (XRD). XRD patterns of NiCo-MOF and Ni-MOF are consistent with previous report [38], while crystallinity of NiCo-MOF decreased compared to Ni-MOF, with Ni^{2+} partially replaced by Co^{2+} (Fig. S1 in Supporting information). Meanwhile, Al-doped $SrTiO_3$ (STO) with excellent crystallinity was successfully prepared (Fig. S1) [39,40]. As shown in Fig. 1, the characteristic peak of NiCo alloy loaded STO (3%-MOF-STO-NH$_3$) is consistent with cubic phase $SrTiO_3$ (JCPDS No. 96-151-2125) without peaks of Ni or Co because of the relatively low loading amount [29]. Specifically, new diffraction peaks could be identified when loading ratio was increased to 40% (40%-MOF-STO-NH$_3$, Fig. S2 in Supporting information), which could be indexed as metal phases Ni (JCPDS No. 96-210-0644) or Co (JCPDS No. 96-901-0969). Due to the close similarity of the characteristic peaks of Ni and Co, there is no obvious splitting peak at 44.2°, 51.5° and 75.8°. Similarly, the XRD pattern of NiCo-MOF annealed with high-temperature ammonia (MOF-NH$_3$ in Fig. 1) also shows similar characteristic peaks of NiCo metal. These results indicate that NiCo-MOF is reduced to metal phase material under high temperature ammonia atmosphere while does not bring other impurities in 3%-MOF-STO-NH$_3$.

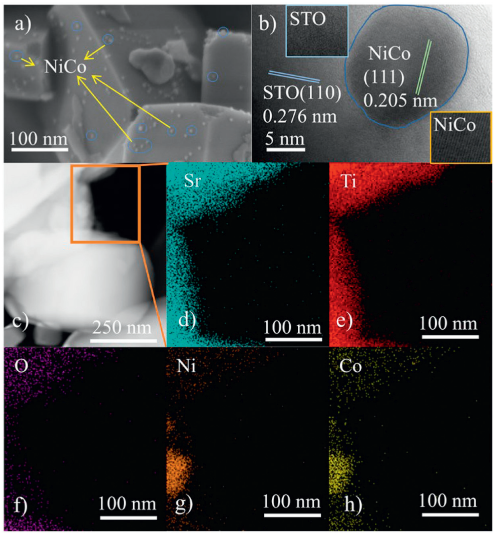

Fig. 2. (a) SEM image, (b) HRTEM image, (c) STEM image and (d-h) corresponding elemental maps of 3%-MOF-STO-NH$_3$.

As shown in the scanning electron microscopy (SEM) images (Fig. S3 in Supporting information), NiCo-MOF exhibits a dandelion-like hollow structure with fluffy protrusions on the surface, and STO exhibits a cubic morphology with diameters in the range of 100–500 nm [11,19]. SEM image in Fig. 2a indicates that the surface of cubic STO is covered with nanoparticles, which could be resulted from the pyrolyzed NiCo-MOF attached on STO under high temperature atmosphere. Further supporting evidence could be found that NiCo-MOF forms a hollow cage when calcined by high temperature air (Fig. S4a in Supporting information) while turns into particles in the reducing ammonia atmosphere (Fig. S4b in Supporting information). In a high-temperature ammonia atmosphere, the NiCo-MOF likely undergoes pyrolysis followed by renucleation, leading to the growth of larger NiCo alloy particles (Fig. S4b). When mixed with NiCo-MOF, the STO acts as a growth platform for the NiCo alloy, facilitating the formation of fine nanoalloy particles on its surface (Fig. 2a). The presence of STO significantly inhibits the aggregation of NiCo alloy into larger particles during its growth. This explains why the NiCo-MOF tends to form larger particles in an ammonia atmosphere but grows as fine nanoalloy particles on the STO surface when coexisting with STO. Further detailed studies are needed to fully understand the growth mechanism. High-resolution transmission electronic microscopy (HRTEM) and scanning transmission electronic microscopy (STEM) images further demonstrate the existence and distribution of Ni, Co on the surface of STO (Figs. 2b-h). The lattice spacing with distances of 0.276 and 0.205 nm could be well indexed to the (110) plane of STO [19] and (111) planes of Ni, Co [29], respectively. Noting that Co doping enters the lattice of Ni, the lattice spacing of NiCo-alloy is larger than Ni (0.203 nm). Further, STEM and corresponding elemental maps of 3%-MOF-STO-NH$_3$ indicate that Ni and Co are spatially distributed uniformly in the NiCo-alloy on the surface of STO. The inductively coupled plasma mass spectrometry (ICP-MS) is used to determine the Ni and Co concentrations in 3%-MOF-STO-NH$_3$. The results indicate that the Ni and Co contents

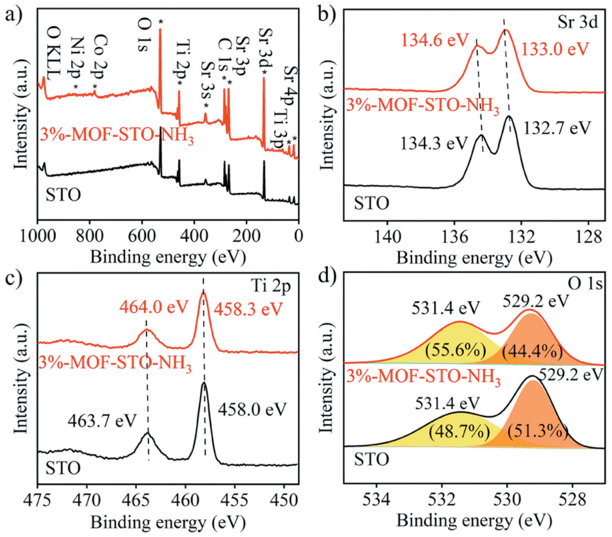

Fig. 3. (a) Survey-scan XPS spectra, high resolution XPS spectra of (b) Sr 3d, (c) Ti 2p and (d) O 1s orbitals for STO and 3%-MOF-STO-NH_3.

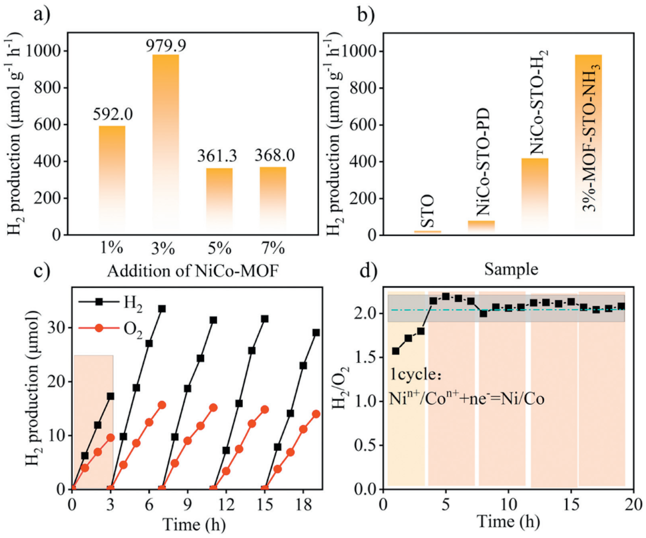

Fig. 4. Photocatalytic activity for H_2 evolution of (a) x%-MOF-STO-NH_3 (x = 1, 3, 5, 7). (b) STO with different loading methods for NiCo-alloy. (c) Stability test of 3%-MOF-STO-NH_3. (d) Molar ratio of hydrogen to oxygen.

are determined to be 1.14 wt% and 1.21 wt%, respectively. The above results show that NiCo-alloy is successfully prepared and loaded on the surface of STO.

XPS spectra were recorded and shown in Fig. 3. For bare STO, only Sr, Ti, O and adsorbed C elements were detected, while 3%-MOF-STO-NH_3 revealed additional signals of Co and Ni elements, further indicating the successful preparation of NiCo-alloy in 3%-MOF-STO-NH_3. In Fig. 3b, the binding energies of Sr $d_{3/2}$ and $3d_{5/2}$ orbitals STO appear at 134.4 and 132.7 eV [41,42], and the peaks located at 463.7 and 458.0 eV are attributed to the $2p_{1/2}$ and $2p_{3/2}$ orbitals of Ti (Fig. 3c). After loading the NiCo-alloy on the surface of STO, the Sr 3d and Ti 2p orbitals are shifted to high binding energy by ~0.3 eV, indicating the potential electron-transfer from STO to NiCo-alloy [43]. In Fig. 3d, the O 1s high resolution XPS spectrum of STO and 3%-MOF-STO-NH_3 can be fitted with two peaks at 529.2 and 531.4 eV, which are attributed to lattice oxygen and surface adsorbed hydroxyl groups (H–O–H), respectively [13,44]. After loading NiCo-alloy, the proportion of hydroxyl groups changed from 48.7% to 55.6%, indicating that the loading of NiCo-alloy is conducive to increasing the hydroxyl group content on the surface of STO, which is beneficial to the hydrogen evolution reaction [13,45]. The significant enhancement of the Fourier transform infrared (FTIR) spectra (Fig. S5 in Supporting information) at 3446 cm^{-1} proves that the 3%-MOF-STO-NH_3 surface is more susceptible to adsorption of hydroxyl groups (H–O–H). The peaks at 855.5 and 873.5 eV in Fig. S6a (Supporting information) are attributed to Ni^{2+} [46,47], while the peaks located at 780.6 and 796.2 eV in Fig. S6b (Supporting information) belong to Co^{3+}[48]. Due to the easily oxidized surface of the small size metal particles and XPS could only reflect the chemical state within depth of several nanometers from the materials, the signals of Ni^0 and Co^0 did not emerge in the data fitting process [49]. It is worth noting that the characteristic peaks of Ni^0 and Co^0 appeared in the XPS spectra of NiCo-MOF after ammonia annealing, which further indicates that NiCo-MOF can be used as a precursor for the preparation of alloy (Figs. S6c and d in Supporting information). During the photocatalytic reaction, the partially oxidized NiCo-alloy on the surface of STO could be quickly reduced by photogenerated electrons and serve as hydrogen-production reactive sites, which will be reflected in the subsequent photocatalytic performance test.

The photocatalytic performance of as-prepared samples was investigated by overall water splitting. Fig. S7a (Supporting information) records the photocatalytic activity for H_2 evolution of STO and MOF-STO treated with different ways. H_2-evolution rates of MOF-STO-AIR, MOF-STO-AIR-NH_3, and 1%-MOF-STO-NH_3 under full spectrum irradiation were 85.2, 296.4, and 592.0 μmol g^{-1} h^{-1}, which were 4.2, 14.5, and 29.0 times as that of STO, respectively.

Compared to samples prepared using Ni-based MOF as a precursor, the sample synthesized using NiCo-MOF as a precursor exhibit superior catalytic performance (Fig. S7b in Supporting information), highlighting the enhanced catalytic properties of the alloy. As XRD results show that MOF can be reduced to metal phase material under high temperature ammonia atmosphere, alloy nanoparticles attached to the STO surface *via* same procedure could promote the photocatalytic performance. With further optimization on the loading amount of cocatalyst (Fig. 4a), the highest rate of photocatalytic H_2 evolution was achieved when the NiCo-MOF addition was 3 wt%, with apparent quantum yield of 11.9% at 350 ± 10 nm and activity of 979.9 μmol g^{-1} h^{-1}, which was 48.0 times as that of STO. To verify the synergistic catalytic effect of bimetallic co-catalysts, STO loaded with single-metal and bimetallic co-catalysts by *in-situ* photodeposition (NiCo-STO-DP) and H_2-annealing (NiCo-STO-H_2) were respectively prepared for comparison. Cocatalyst from photodeposition method did not exhibit the bimetallic synergistic catalytic effect, probably due to the fact that simultaneous photodeposition of both metals did not result in the formation of NiCo-alloy (Fig. S7c in Supporting information). The samples prepared by H_2-annealing again confirmed that the Ni, Co bimetallic co-catalyst could promote the photocatalytic reaction compared with the single metal loading (Fig. S7d in Supporting information). In contrast, the loading of bimetallic alloy co-catalysts on the surface of STO with NiCo-MOF as precursors exhibited higher water splitting performance, which was 2.5 times higher than NiCo-STO-H_2 (Fig. 4b).

The stability test results of 3%-MOF-STO-NH_3 are shown in Fig. 4c. H_2 evolution of 3%-MOF-STO-NH_3 did not decrease significantly in 4 cycles (16 h), indicating 3%-MOF-STO-NH_3 exhibited excellent photocatalytic stability. XRD and high resolution XPS spectra revealed that the crystal structure and chemical state of 3%-MOF-STO-NH_3 did not change significantly before and after water splitting test, which verified the stability of the catalysts (Fig. S8 in Supporting information). The molar ratio of H_2/O_2 in the first cycle is less than 2:1 (Fig. 4d), while the hydrogen generation in the first

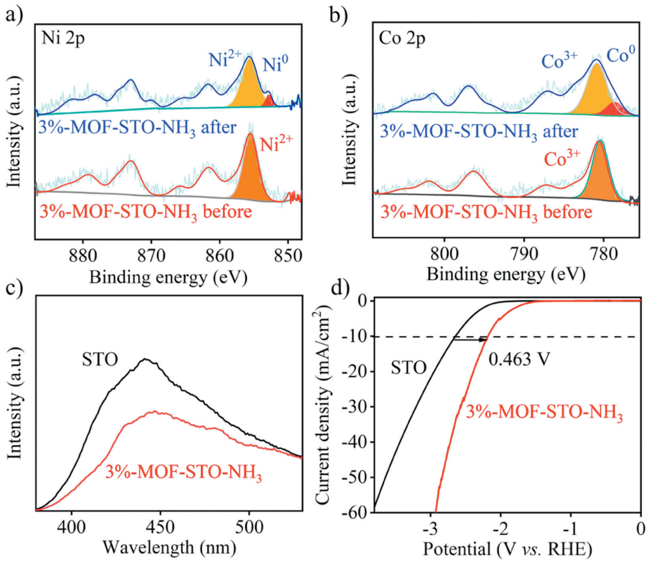

Fig. 5. High resolution XPS spectra of (a) Ni 2p and (b) Co 2p orbitals for 3%-MOF-STO-NH_3 irradiated before and after, (c) photoluminescence spectra, (d) LSV curves of STO and 3%-MOF-STO-NH_3.

cycle is lower than that in the second cycle, indicating the hydroxyl oxides on the surface of the NiCo-alloy are electronically reduced and reconverted to NiCo-alloy during the first cycle. This process can be regarded as the co-catalyst activation stage. The NiCo-alloy acts as a hydrogen evolution reaction (HER) active site, so the oxidized hydroxyl oxides on the surface of the alloy tend to be reduced. This also coincides with high resolution XPS spectra of Ni and Co 2p orbital (Figs. 5a and b). After the first cycle, the high resolution spectra of Ni and Co 2p orbitals of 3%-MOF-STO-NH_3 showed peaks of Ni^0 and Co^0, respectively, which indicated that Ni^{2+} and Co^{3+} on the surface of NiCo alloy are reduced by photogenerated electrons. The molar ratio of H_2/O_2 produced by photocatalytic water splitting was close to 2:1 after the first cycle when the co-catalyst was completely converted to NiCo-alloy.

As shown in Fig. 5c, the emission peaks of photoluminescence spectra at ~445 nm for both samples are ascribed to the recombination of carriers [11]. In contrast, the fluorescence intensity of STO is significantly higher than that of 3%-MOF-STO-NH_3, indicating that the loading of NiCo-alloy facilitates carrier migration. The increase in fluorescence lifetime indicates an improvement in carrier separation efficiency upon loading of NiCo alloy (Fig. S9 in Supporting information). Meanwhile, the carrier migration of the prepared samples was further investigated using electrochemical impedance spectroscopy and linear sweep voltammetry (LSV) curve. The smaller Nyquist semicircle of 3%-MOF-STO-NH_3 indicates a greater contribution to enhanced carrier migration and separation (Fig. S10 in Supporting information). Meanwhile, LSV curve of HER showed that the overpotential of STO after loading NiCo-alloy was lower than that of STO (~0.463 V at 10 mA/cm^2), indicating that the alloy co-catalyst facilitated the HER (Fig. 5d). As shown in Fig. S11 (Supporting information), the UV–vis absorption spectrum depicts the absorption of as-prepared samples for different wavelengths of light. The absorption edge of all samples was 380 nm, indicating that the loading of the co-catalyst did not affect the band gap of STO. The absorption edge of 3%-MOF-STO-NH_3 in the visible region is enhanced, which demonstrates the successful surface loading of bimetallic alloys.

The charge density distribution and the direction of electron transfer at the interface between NiCo-alloy and STO were then revealed by density functional theory (DFT). As shown in Fig. 6a, the interfaces of NiCo accumulate electrons indicated by a yellow region while electrons in interfaces of STO dissipate as indicated by blue. To further investigate the promotion of HER on the STO surface by bimetallic alloy co-catalysts, the charge density distribution of an additional electron on the (100) surface of NiCo loaded STO was calculated to simulate the distribution of photogenerated electrons on the surface of the alloy-loaded photocatalysts when STO was excited by light (Fig. 6b). Calculated results indicated the electrons generated by optical excitation of STO tend to accumulate on the surface of NiCo-alloy with high work function on the surface of STO. The plane-averaged charge density difference $\Delta\rho(Z)$ parallel to the planes of STO and NiCo-alloy (Fig. 6c), confirming an obvious charge transfer from STO to NiCo. According to the Mott-Schottky testing (Fig. S12 in Supporting information), the flat band potentials for STO and 3%-MOF are −0.514 and −0.397 eV, respectively. The significant positive shift in flat band potential originates from the electron redistribution during the formation of heterojunction between STO and NiCo alloy. Further DFT calculations show that the bimetallic alloy on the STO (110) surface is more favorable for H adsorption compared to a single metal (Fig. 6d), which has the advantage of facilitating the HER. Meanwhile, Ni sites in NiCo-alloy are more conducive to H adsorption compared to Co sites, suggesting that HER is better suited to the Ni sites.

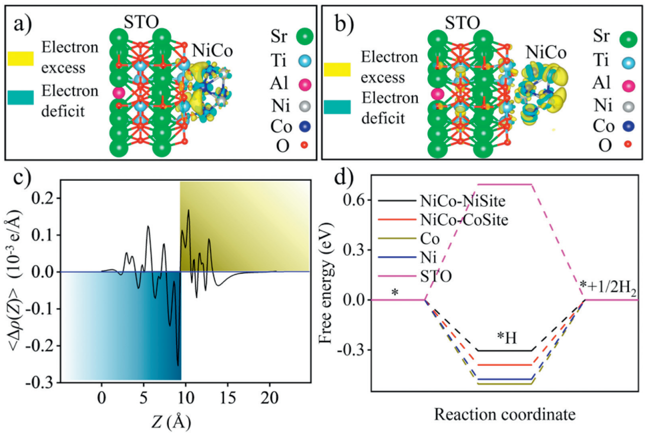

Fig. 6. (a) The charge density difference and (b) electron distribution of STO loading NiCo-alloy during simulated irradiation. (c) Planar-averaged differential charge density $\Delta\rho(Z)$ along Z direction of STO and NiCo interfacial heterojunction. (d) The free energy diagram of H atom on different site.

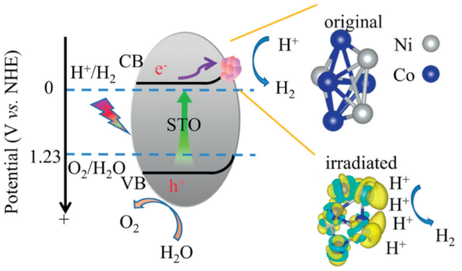

Fig. 7. Schematic diagram of band structure, expected charge separation and simulated HER processes of 3%-MOF-STO-NH_3 (yellow areas indicate electron enrichment).

Both experimental and theoretical calculations show that bimetallic alloy have more prominent catalytic performance than single-metal co-catalysts. The detailed photocatalytic reaction mechanism was proposed and shown in Fig. 7. On the one hand, NiCo-alloy with higher work functions cause electrons to be transferred from the STO surface to NiCo-alloy after forming heterojunctions with STO. The electrons generated by photoexcitation migrate to the STO conduction band firstly and then transfer to the NiCo-alloy, which effectively promotes the spatial separation of carriers and reduces the carrier composite. On the other hand, the bimetallic alloy co-catalysts exhibit enhanced suitability for the HER. Ni sites in NiCo-alloy adsorb H and react reduction reaction with the participation of electrons to form H_2. After the formation of NiCo-alloy, the H adsorption energy of Ni sites was significantly reduced, which was more suitable for H adsorption and HER.

In summary, we successfully prepared NiCo alloy co-catalysts with bimetallic MOF as precursor for photocatalytic overall water splitting. The distribution of metal elements in the bimetallic MOF is more rational, which will better function the synergistic effects of bimetallic alloy. Meanwhile, the introduction of Co facilitates H adsorption at the Ni site, which is beneficial for further H_2 evolution processes. 3%-MOF-STO-NH_3 could produce hydrogen and oxygen for photocatalytic overall water splitting in stoichiometric ratio, with apparent quantum yield of 11.9% at 350 ± 10 nm. This work provides a solution for synthesizing and loading economical and efficient alloy co-catalysts.

Declaration of competing interest

The authors declare that they have no known competing financial interests or personal relationships that could have appeared to influence the work reported in this paper.

CRediT authorship contribution statement

Liang Dong: Writing – review & editing, Writing – original draft, Visualization, Validation, Resources, Methodology, Investigation, Funding acquisition, Formal analysis, Data curation. **Jingkuo Qu:** Writing – review & editing, Software, Investigation, Formal analysis, Data curation. **Tuo Zhang:** Investigation. **Guanghui Zhu:** Investigation. **Ningning Ma:** Conceptualization. **Chang Zhao:** Conceptualization. **Yi Yuan:** Conceptualization. **Xiangjiu Guan:** Writing – review & editing, Supervision, Resources, Funding acquisition, Conceptualization. **Liejin Guo:** Writing – review & editing, Supervision, Resources, Funding acquisition, Conceptualization.

Acknowledgments

This work is supported by the Basic Science Center Program for Ordered Energy Conversion of the National Natural Science Foundation of China (No. 52488201), the National Natural Science Foundation of China (No. 52376209), the China Postdoctoral Science Foundation (Nos. 2020T130503 and 2020M673386), and China Fundamental Research Funds for the Central Universities.

Supplementary materials

Supplementary material associated with this article can be found, in the online version, at doi:10.1016/j.cclet.2024.110397.

References

[1] Q. Wang, K. Domen, Chem. Rev. 120 (2020) 919–985.
[2] X.L. Chen, J.J. Zhao, G.S. Li, D.Q. Zhang, H.X. Li, Energy Mater. 2 (2022) 200001.
[3] H. Nishiyama, T. Yamada, M. Nakabayashi, et al., Nature 598 (2021) 304–307.
[4] Y.M. Zhang, X.S. Wang, X.H. Ren, et al., Chem. Eng. J. 456 (2023) 141032.
[5] Z. Jiang, Z. Ye, W.F. Shangguan, Front. Energy 16 (2022) 49–63.
[6] B. Wang, B. An, X.Q. Li, S.H. Shen, Front. Energy 18 (2023) 101–109.
[7] C.M. Pelicano, M. Saruyama, R. Takahata, et al., Adv. Funct. Mater. 32 (2022) 2202987.
[8] L.J. Guo, Y.B. Chen, J.Z. Su, M.C. Liu, Y. Liu, Energy 172 (2019) 1079–1086.
[9] H. Lyu, T. Hisatomi, Y. Goto, et al., Chem. Sci. 10 (2019) 3196–3201.
[10] T. Takata, J.Z. Jiang, Y. Sakata, et al., Nature 581 (2020) 411–414.
[11] L. Tian, X.J. Guan, Y.C. Dong, et al., Environ. Chem. Lett. 21 (2023) 1257–1264.
[12] D.H.K. Murthy, V. Nandal, A. Furube, et al., Adv. Energy Mater. 13 (2023) 2302064.
[13] R.H. Li, T. Takata, B.B. Zhang, et al., Angew. Chem. Int. Ed. 62 (2023) e202313537.
[14] F. Fang, R.Z. Xu, Z.Y. Su, et al., Catal. Lett. 153 (2023) 1083–1088.
[15] K. Chen, J. Xiao, J.J.M. Vequizo, et al., J. Am. Chem. Soc. 145 (2023) 3839–3843.
[16] J.X. Bai, B.C. Lu, Q. Han, Q.S. Li, L.T. Qu, ACS Appl. Mater. Interfaces 10 (2018) 38066–38072.
[17] J.D. Xiao, S.J. Nishimae, J.J.M. Vequizo, et al., Angew. Chem. Int. Ed. 61 (2022) e202116573.
[18] P. Zhou, I.A. Navid, Y. Ma, et al., Nature 613 (2023) 66–70.
[19] S.C. Zong, L. Tian, X.J. Guan, et al., J. Colloid Interface Sci. 606 (2022) 491–499.
[20] X.L. Liu, X.M. Yang, J.W. Cui, et al., ACS Catal. 21 (2023) 14314–14323.
[21] X.H. Ma, W.J. Li, H.D. Li, et al., J. Colloid Interface Sci. 639 (2023) 87–95.
[22] Q. Lan, S.J. Jin, B.H. Yang, et al., Trans. Tianjin Univ. 28 (2022) 214–225.
[23] H.Q. An, M. Li, R.D. Liu, Z.R. Gao, Z. Yin, Chem. Eng. J. 382 (2020) 122953.
[24] J.C. Hao, H. Zhu, Y.Z. Li, et al., Chem. Eng. J. 404 (2021) 126523.
[25] Y.F. Zhang, S.J. Park, Chem. Eng. J. 369 (2019) 353–362.
[26] B. Wang, S. He, L.L. Zhang, et al., Appl. Catal. B: Environ. 243 (2019) 229–235.
[27] S. Ibrahim, I. Majeed, Y.H. Qian, et al., Inorg. Chem. Front. 5 (2018) 1816–1827.
[28] X. Han, D.Y. Xu, L. An, et al., Appl. Catal. B: Environ. 243 (2019) 136–144.
[29] Z.J. Li, X.H. Wang, W.L. Tian, A.L. Meng, L.N. Yang, ACS Sustain. Chem. Eng. 7 (2019) 20190–20201.
[30] S.B. Chen, M.L. Li, S.Y. Yang, X. Li, S.S. Zhang, Appl. Surf. Sci. 492 (2019) 571–578.
[31] J.C. Shen, C.H. Luo, S.S. Qiao, et al., Adv. Funct. Mater. 34 (2023) 2309056.
[32] P. Balasubramanian, H. Khan, J.H. Baek, S.H. Kwon, Chem. Eng. J. 471 (2023) 144378.
[33] L.Q. Li, H.F. Qiu, Y.P. Zhu, et al., Appl. Catal. B: Environ. 331 (2023) 122710.
[34] L.K. Wu, W.Y. Wu, J. Xia, et al., J. Mater. Chem. A 5 (2017) 10669–10677.
[35] I. Majeed, U. Manzoor, F.K. Kanodarwala, et al., Catal. Sci. Technol. 8 (2018) 1183–1193.
[36] U. Caudillo-Flores, M.J. Muñoz-Batista, M. Fernández-García, A. Kubacka, Appl. Catal. B: Environ. 238 (2018) 533–545.
[37] Y.X. Liu, Z.X. Sun, Y.H. Hu, Chem. Eng. J. 409 (2021) 128250.
[38] S.W. Gao, Y.W. Sui, F.X. Wei, et al., J. Colloid Interface Sci. 531 (2018) 83–90.
[39] X.J. Guan, L.J. Guo, ACS Catal. 4 (2014) 3020–3026.
[40] Y.L. Ham, T. Hisatomi, Y. Goto, et al., J. Mater. Chem. A 4 (2016) 3027–3033.
[41] D. Yang, Y.Y. Sun, Z.W. Tong, Y.H. Nan, Z.Y. Jiang, J. Hazard. Mater. 312 (2016) 45–54.
[42] H. Bantawal, U.S. Shenoy, D.K. Bhat, Appl. Surf. Sci. 513 (2020) 145858.
[43] S.C. Zong, L. Tian, X.J. Guan, et al., Surf. Interfaces 48 (2024) 104285.
[44] Y.S. Zhu, P.A. Salvador, G.S. Rohrer, Chem. Mat. 28 (2016) 5155–5162.
[45] S.H. Wei, X.X. Xu, Appl. Catal. B: Environ. 228 (2018) 10–18.
[46] J. Wang, Y.A. Xie, Y.Y. Yao, et al., J. Mater. Chem. A 5 (2017) 14758–14762.
[47] D.Q. Gao, J.Y. Zhang, T.T. Wang, et al., J. Mater. Chem. A 4 (2016) 17363–17369.
[48] Q. Zhang, P.J. Yang, H.X. Zhang, et al., Appl. Catal. B: Environ. 300 (2022) 120729.
[49] X.Y. Lu, X. Tan, Q.R. Zhang, et al., J. Mater. Chem. A 7 (2019) 12154–12165.